# A data-driven machine learning approach for predicting the failure of unidirectional CFRP composites under triaxial loading

Jiayun Chen [1, 2, *], Lei Wan [1,*], Yaser Ismail [3], Jianqiao Ye [4], Dongmin Yang [1, †]

[1] Institute for Materials and Processes, School of Engineering, University of Edinburgh, Edinburgh EH9 3FB, UK
[2] College of Mechanical and Vehicle Engineering, Hunan University, Changsha 410082, PR China
[3] Groundforce Shorco, Gildersome, Leeds LS27 7HJ, UK
[4] Department of Engineering, Lancaster University, Lancaster LA1 4YW, UK

## Abstract

This study presents a machine learning approach based on an artificial neural network (ANN) for the failure prediction of IM7/8552 unidirectional (UD) composite lamina under triaxial loading. The ANN is trained offline by numerical data from a representative volume element (RVE) based, high fidelity micromechanical model using the finite element method (FEM). The RVE adopts identified constituent parameters from inverse analysis and calibrated interface strengths form uniaxial and biaxial tests. A hybrid loading strategy is proposed for the RVE under triaxial loading to obtain the failure points on sliced surfaces whilst maintaining the constant stress at different surfaces. Verification tests and comparisons between different machining learning approaches are carried out, with the ANN standing out due to its higher accuracy. It has been found that the ANN algorithm is surprisingly robust in the failure prediction of the UD lamina when subjected to different triaxial loading conditions, with over 97.5% accuracy being achieved by the shallow ANN model, where only two hidden layers and 560 samples are used. The predicted 3D failure surface based on trained ANN model has an elliptical paraboloid shape and shows an extremely high strength in biaxial compression. The approach could be used to inform the modification of existing failure criteria and to propose ANN-based failure criteria.

**Keyword:** Machine learning; UD lamina; Failure prediction; Finite element modelling; Representative volume element; Triaxial loading.

## 1. Introduction

Carbon Fibre Reinforced Polymer (CFRP) composites are widely utilised in aerospace, wind energy and automotive industries due to their high ratio of strength/stiffness to weight. However, the complex failure mechanisms of the unidirectional (UD) CFRP composite lamina are still undergoing investigation, since the damage initiation and propagation mechanisms vary at different length scales under different loading conditions, in particular under the multi-axial loading.

Currently, a number of failure theories and models have been proposed, including strain-based [1,2], stress-based [3–5] and phenomenological models [6–8]. The World Wide Failure Exercises (WWFEs) have been conducted to assess the robustness of those aforementioned state-of-art failure theories, based on their predictive capabilities of the failure strength of FRP composite lamina and laminates subjected to various loading conditions [9–11]. However, it was concluded that no failure theory/model can accurately handle all of the experimental testing cases and there is no identical failure predictions

† Corresponding author. Email: Dongmin.Yang@ed.ac.uk

* These two authors contribute equally.

between any two failure theories [12]. Since then, specific failure modes (i.e. tension, shear and compression failures) have been incorporated into the newly developed generalised failure theories [13,14], with the appreciation that such criterion gives better predictions of biaxial failure in the FRP composites during the WWFEs [6].

The mechanical properties of CFRP composite materials are largely dependent on the material properties of fibres and matrix, fibre spatial distribution as well as void size and position. Besides, at the microscale level, the characteristics of the interfacial bonding between the fibres and matrix and the mechanism of loading transfer between different constituents have a significant influence on the ultimate mechanical performance [15], especially in multiaxial stress states. Thus, it remains challenging to develop a universal failure criterion for UD lamina to cover the aforementioned factors, resulting in more difficulties for the failure prediction of composite materials under multiaxial stresses. From the perspective of experimental testing, the triaxial test method is not well developed and it is difficult to measure the triaxial deformation of a specimen, which leads to the scattering of measured data. As a result, establishing a reliable and universal failure criterion with experimental validations, even for a UD composite lamina, is still a challenging task.

Over the past decade, computational micromechanics has been applied to investigate the deformation and failure mechanisms of the composites by means of a representative volume element (RVE) within the framework of finite element method (FEM). By using the RVE modelling technique, the actual fibre size and spatial distribution, and the interface between fibres and matrix can be explicitly taken into account in a three-phase model. In addition, the evolution of stresses and strains within the RVE subjected to various loads can be captured, which provides more information of the damage onset and propagation in composite materials in addition to the ultimate failure strength prediction [16]. Micromechanics-based RVE modelling has been successfully applied to study the progressive failure of CFRP composite materials under multiaxial loads, such as combined transverse tension/compression and out-of-plane shear [17,18], biaxial transverse tension/compression and in-plane shear [19–21] and combined transverse compression and axial tension [22]. In the RVE model, the fibre/matrix interface properties play a significant role and a cohesive zone model (CZM) is usually employed to capture the mechanical response of the fibre/matrix interface. In the linear part of the CZM before damage, an empirical initial penalty stiffness $K_i$ ($10^5$ GPa/mm) was adopted [16–18,20,21], which was believed to be large enough to ensure the displacement and stress continuity at the interface [21]. However, it was reported in [22] that the average Young's modulus of the interphase between fibres and matrix is five to nine times larger than the one of the bulk resin matrix [14]. In our previous work [19], identified interface parameters based on a Kriging metamodel [23] were adopted in the RVE modelling of a UD composite lamina subjected to combined transverse and in-plane shear stress state and good agreements were found when compared to three popular failure criteria. The influences of the interface strength on the progressive failure mechanisms of the composite lamina was investigated and it was concluded that the Tsai-Wu failure criterion predicted more neutrally in all cases, mainly due to its general mathematical formulation.

Commented [YJ1]: ???

The aforementioned studies using computational micromechanics have demonstrated the capability of the RVE models for the failure analysis of composite materials under multiaxial loadings. Also, it was found in [19] that the average computing time of a biaxial loading case with the RVE modelling (in ABAQUS/Explicit) lies in 6-8 hours, which makes possible the generation of large sets of 'virtual experimental' data for any loading conditions within a reasonable period of time.

On the other hand, with the rapid development of computing power, machine learning (ML) technique is gaining wider applications in predicting the failure of materials and structures. It is well known that

a ML algorithm relies on a sufficiently large number of data for training to produce reliable and accurate results, while obtaining such big data from experiments only would be time-consuming and expensive. Nevertheless, with increasing computing power, such as high-performance computing (HPC), enough data sets can be possibly acquired from numerical simulations within a few days or months. This has enabled some encouraging progresses in recent years. For example, Sujith and Jong-Su [24] used lasso regression to predict the failure mode and the shear strength of reinforced concrete beam-column joints; Honglan and Henry [25] compared the performance of different ML algorithms for identifying the in-plane failure modes of concrete frames; Xin et al. [26] used neural network model to predict the failure strength of the woven composites; Xing et al. [27] adopted the regression trees and neural networks to identify a small-scale fracture toughness; Shibo et al. [28] built a surrogate model in together with a neural network model to predict the stress and damage evolution.

However, to the authors' best knowledge, few studies were focused on the failure prediction of composite materials subjected to triaxial loads using the combination of ANN and high-fidelity RVE models. Therefore, in this study a RVE model of IM7/8552 UD lamina was built using identified constituent parameters by an ANN algorithm. After calibrating the interface strengths under uniaxial loads and validating the failure predictions under biaxial loads, the RVE model was applied to predict the failure points of the composite lamina subjected to triaxial loads. Especially a hybrid loading strategy is proposed to eliminate the Poisson's effect occurred in displacement loadings and to determine the failure points of composites under triaxial loads. The failure prediction of composite materials was regarded as a classification problem in this study, and three ML algorithms, including ANN, logistic regression and support vector machine (SVM), were evaluated. ANN was chosen for training and validations by the failure data generated from the RVE model under triaxial loads, considering of its prediction accuracy and the nonlinearity of the problem concerned.

The paper is organised with the following structure. In Section 2, the micromechanics-based FE model is introduced, including the details of the RVE, periodic boundary conditions and loading paths. In Section 3, the performance of different ML algorithms for failure prediction is compared using the theoretical data from the Tsai-Wu criteria. In Section 4, the RVE model is calibrated and validated by experiments. In Section 5, the numerical data from the RVE modelling are collected and used to train the ANN model. Finally, conclusions are drawn in Section 6.

## 2. Computational micromechanics-based FE modelling using RVEs

### 2.1 3D FEM RVE model

Computational micromechanical analysis is generally performed on the RVEs of the UD composite laminae. The number of fibres within a RVE should be large enough to possess the same mechanical properties as the macroscopic material. It has been proved 50 fibres would be sufficient to represent the microstructure of a UD composite lamina [16], and small enough to maintain a reasonable computing time. Moreover, the volume fraction was set as 60% and the average fibre diameter is considered to be 7 μm, based on the experimental measurement of the IM7/8552 composite [29]. A discrete element method-based approach, developed in our previous wok by combining experimental data and an initial periodic shaking algorithm [30], was adopted to generate the random distribution of fibres in 2D. The 3D RVE model of the UD composite lamina was created by extruding the 2D model along the fibre direction. The microstructure of the RVE is idealised as the dispersion of circular fibres randomly distributed in the matrix. It was found by Totry et al. [17] that the RVE depth has an insignificant effects on the transverse properties obtained from the finite element simulations. Thus, a thickness of 5 μm for the RVE was selected in this study as a compromise between the accuracy of the results and the computing efforts, resulting in a RVE of 50 μm ×50μm× 5μm. An

identified interface thickness using an artificial neural network from our previous work [31] was utilised in the construction of the 3D RVE model. More details will be described later in Section 4.1.

The fibres and the matrix in the RVE model were discretised using hexahedral solid elements with reduced integration scheme (C3D8R) and some wedge elements (C3D6) inserted into some regions that are difficult to be meshed using the hexahedral elements. The interphase was meshed using the first-order cohesive elements (COH3D8), as shown in Fig. 1. Approximately 20,000 elements were utilised to capture the stress distribution and material deformation between neighbouring fibres at a reasonable computational cost. Node positions on opposite faces of the RVE were identical to allow periodic boundary conditions. Mass scaling was employed to accelerate the numerical simulations in ABAQUS/Explicit. A ratio of the kinetic energy over the internal energy of the system is a commonly used parameter to determine whether the mass scaling has significant influence on the numerical results, and it is well recognised that any ratio less than 10% could be seen as insignificant [14]. Therefore, the stable time increment was set to be $5\times10^{-6}$ s in this study. The linear bulk viscosity and the quadratic bulk viscosity parameter were set to be 0.06 and 1.2 in ABAQUS/Explicit, respectively.

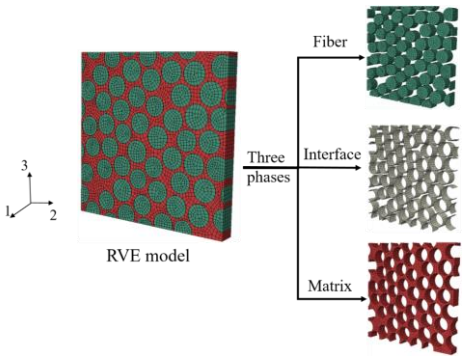


Fig 1. The 3D RVE model with three phases

2.2 Constitutive models of the three phases

In this study, fibre damage is not considered as it is assumed that there is no direct stress in the fibre direction. The carbon fibres were modelled as linearly elastic, transversely isotropic solids, and their material properties are listed in Table 1. The polymeric matrix was modelled as isotropic elasto-plastic. It has been found that the hydrostatic stress has significant influences on the mechanical behaviour of polymer [32], and exhibits a completely different behaviour when subjected to various simple uniaxial loading conditions, such as brittle in tension while plastic in compression and shear [33]. These characteristics of polymers were considered in the failure analysis of composite materials under multiaxial stress states, by means of the extended Drucker-Prager (D-P) yield model associated with a ductile damage criterion [19], the modified Drucker-Prager plastic damage model [20] and the elasto-plastic with isotropic damage constitutive model, proposed by Melro et al. [34]. In order to generate a large amount of numerical data from the RVE model efficiently and to avoid the change of hardening pattern in the extended D-P model at the damage mode transition point [19], the modified D-P plastic damage model implemented in ABAQUS was adopted. The constitutive model is based on the yield function proposed by Lubliner et al. [35] associated with modifications accounting for damage evolution subjected to tensile and compressive loads [36]. The yield surface of epoxy is given by the modified Drucker–Prager yield function

$$\Phi(I_1, J_2, \sigma_I, \beta, \alpha) = \frac{1}{1-\alpha}\left(\sqrt{3J_2} + \alpha I_1 + B\langle\sigma_I\rangle\right) - \sigma_{myc} = 0, \quad (1)$$

where $I_1$ is the first invariant of the stress tensor, $J_2$ the second invariant of the deviatoric stress tensor, $\alpha$ the pressure-sensitivity parameter, $\sigma_I$ the maximum principal stress, <> the Macaulay brackets that returns the argument when it's positive or zero, and $B$ is a function of the tensile and compressive yield strengths ($\sigma_{myt}$ and $\sigma_{myc}$), which reads

$$B = \frac{\sigma_{myt}}{\sigma_{myc}}(1-\alpha) - (1+\alpha), \quad (2)$$

wherein $\alpha$ can be determined according to $\tan\beta = 3\alpha$ from the internal friction angle of the material ($\beta$), which controls the hydrostatic pressure dependence of the plastic behaviour of the material.

After onset of damage under tensile loads, the quasi-brittle behaviour is determined by an exponential law, characterised by a damage variable for the fracture energy $G_m$. For the behaviour of matrix under compressive loads, perfect plastic was assumed, which is schematically illustrated in Fig. 2(a). More details about the constitutive model and the numerical implementation can be found in [20].

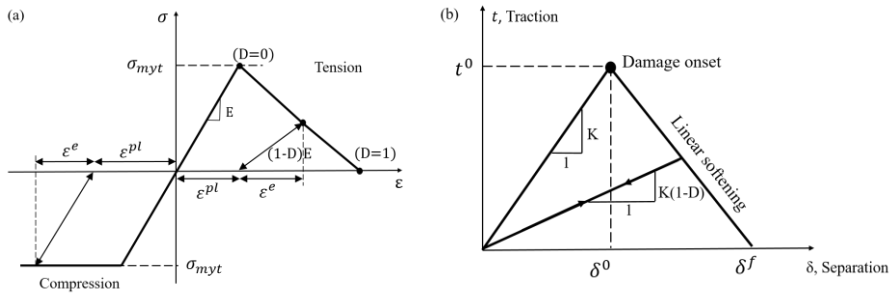


Fig 2. (a) Schematic of the modified Drucker-Prager damage-plastic model for the epoxy matrix; (b) Traction-separation law of the fibre/matrix interface.

The mechanical behaviour of the interface between fibres and matrix was modelled by a cohesive zone model (CZM) and governed by the traction-separation law ( see Fig. 2(b)). Damage onset was controlled by a quadratic interaction criterion, while the propagation was determined by the energy-based Benzeggath-Kenane damage criterion, considering the dependence of the fracture energy dissipation on the fracture modes. The interface fracture energy in mode I, $G_{IC}$, is extremely difficult to be measured experimentally, so it is assumed between 2-5 J/m$^2$ [20]. Here in this study, the energy of 2 J/m$^2$ was adopted in the simulations, which has also been adopted in other studies [20,34]. Furthermore, because of the absence of experimental data, it was assumed that the interface fracture energy for the shear mode was equal to the matrix cracking fracture energy, 100 J/m$^2$, which is similar to the one used in [20,36]. More details of this cohesive zone model and its numerical implementation can be found in [19]. It should be noted that in this model, the friction between fibres and matrix after interface failure was not considered, and requires a subroutine in the element based cohesive zone model. The interface properties and the identified parameters can be found in Table 1.

**Commented [YJ2]:** Subroutine for not considering frictions?

Table. 1. Material properties of IM7/8552 composite and identified interface parameters [11,36]

| IM7 fibre properties |
|---|

| $E_1$ (GPa) | $E_2 = E_3$ (GPa) | $\nu_{12}$ | $\nu_{23}$ | $G_{12}$ (GPa) | $G_{23}$ (GPa) |
|---|---|---|---|---|---|
| 287 | 13.399 | 0.29 | 0.48 | 23.8 | 7 |

8552 epoxy properties

| $E$ (GPa) | $\nu_m$ | $\sigma_{myt}$ (MPa) | $\sigma_{myc}$ (MPa) | $G_m$ (J / m$^2$) |
|---|---|---|---|---|
| 4.08 | 0.38 | 99 | 130 | 100 |

Interface properties

| Thickness (mm) | $K_{nn}$ (GPa/mm) | $K_{ss}$=$K_{tt}$ (GPa/mm) | $t_n^0$ (MPa) | $t_s^0 = t_t^0$ (MPa) | $G_{IC}$ (J / m$^2$) | $G_{IIC}$=$G_{IIIC}$ (J / m$^2$) |
|---|---|---|---|---|---|---|
| 0.0001 | 253 | 682 | 45 | 62 | 2 | 100 |

2.3 Boundary and loading conditions

When an RVE is constructed, periodic boundary conditions (PBCs) are necessary to ensure the periodic displacement and traction fields by introducing the following equations for ~~between~~ the nodes of surfaces and their counterparts on the opposite surfaces. The unified PBCs are generally written with displacement vectors $U_1$, $U_2$ and $U_3$ as

**Commented [YJ3]:** With arrows?

$$\begin{cases} \vec{u}(0, x_2, x_3) - \vec{u}(L_1, x_2, x_3) = \overrightarrow{U_1} \\ \vec{u}(x_1, 0, x_3) - \vec{u}(x_1, L_2, x_3) = \overrightarrow{U_2}, \\ \vec{u}(x_1, x_2, 0) - \vec{u}(x_1, x_2, L_3) = \overrightarrow{U_3} \end{cases} \tag{3}$$

where $L_1$ ($i$=1, 2, 3) is the length of the RVE, and $\overrightarrow{U_i}$ (i=1, 2, 3) are the relative displacement between two nodes on the pair of opposite surfaces. Three dummy points are introduced to apply the load, such that it is easy to achieve various loading conditions through the modifications of displacements/loads of these nodes. More details of PBC and its implementation in RVE based modelling are referred to [19,35].

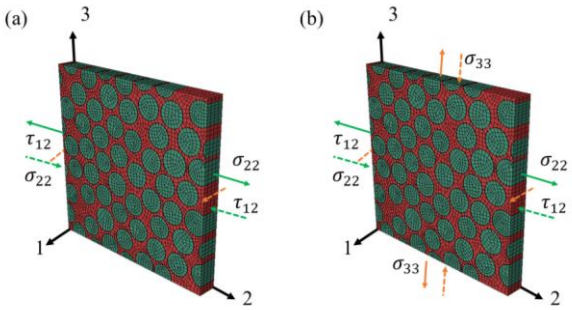


Fig 3. RVE subjected to different loads: (a) uniaxial transverse tension/compression and in-plane shear loadings; (b) biaxial transverse tension/compression and in-plane shear loadings.

Combined uniaxial tension/compression along the $x_2$ axis and longitudinal shear along the fibres ($\sigma_{22}$ and $\tau_{12}$ in Fig 3(a)) were imposed with $\overrightarrow{U_1} = (u_1, 0,0)$, $\overrightarrow{U_2} = (0, \delta_{t/c}, \delta_s)$ and $\overrightarrow{U_3} = (0, 0, u_3)$, where $\delta_c$ and $\delta_s$ are the imposed compressive and shear displacements, respectively. $u_1$ and $u_3$ are regarded as the resultant displacements with the consideration of Poisson's effects, so that the corresponding normal forces acting on the RVE surfaces are zero. The imposed strains were computed from the imposed displacements divided by the corresponding lengths, while the predicted normal and shear stresses were computed from the resultant normal and tangential forces acting on the RVE faces divided by the cross-sectional area.

For triaxial loadings, including biaxial transverse loads perpendicular to the fibres and in-plane shear, the loads were imposed on two dummy nodes in two steps. Here in this study, force loading was introduced throughout these two steps, considering the restriction of Poisson's effects in displacement loading. In the first step, the uniaxial force loading was imposed with $\overrightarrow{U_1} = (u_1, 0,0)$, $\overrightarrow{U_2} = (0, u_2, 0)$, $\overrightarrow{U_3} = (0, 0, u_{3f})$ and $\overrightarrow{F_3} = (0, 0, \pm F_{33})$, where the $u_1$ and $u_2$ are the resultant displacements with the consideration of Poisson's effects, the $\pm F_{33}$ is the concentrated force loaded on the dummy node along the $x_3$ axis and $u_{3f}$ is the resultant displacement due to the concentrated force loading $\pm F_{33}$. By doing so, the transverse stress can be imposed on the cross-section, and needs to be kept constant throughout the second step. In the second step, triaxial loads were imposed with $\overrightarrow{U_1} = (u_1, 0,0)$, $\overrightarrow{U_2} = (0, \delta_{t/c}, \delta_s)$, $\overrightarrow{U_3} = (0, 0, u_{3f})$ and $\overrightarrow{F_3} = (0, 0, \pm F_{33})$, in which the transverse tension/compression and in-plane shear were loaded with displacements on the dummy nodes along $x_2$ axis.

For all the loadings, the displacements and reactions of these dummy nodes were obtained to determine the stress–strain curves under the transverse, shear and combined loads. They were also used to derive the corresponding material stiffness and strength, and plot the failure loci in the stress space ($\sigma_{33}$-$\sigma_{22}$-$\tau_{12}$). The average computing times were around 6 hours and 15 hours for the biaxial and triaxial loading cases, respectively, using a single CPU for each job on the Eddie HPC platform at the University of Edinburgh.

## 3. Verification tests

### 3.1 Theoretical data

In order to verify and compare ML methods, the Tsai-Wu failure criterion [37] described in Eq. (4) was adopted as a benchmark to provide theoretical data sets for training and validation. The Tsai-Wu criterion was selected because it includes all stress components with a concise expression and performs generally well in comparing theoretical failure criteria and RVE based simulations under biaxial loads [19].

$$F = F_{11}\sigma_{11}^2 + F_{22}\left(\sigma_{22}^2 + \sigma_{33}^2\right) + \left(2F_{22} - F_{44}\right)\sigma_{22}\sigma_{33} + 2F_{12}\sigma_{11}\left(\sigma_{22} + \sigma_{33}\right) + F_1\sigma_{11} + F_2(\sigma_{22} + \sigma_{33}) + F_{44}\tau_{23}^2 + F_{66}\left(\tau_{13}^2 + \tau_{12}^2\right), \quad (4)$$

where $F_i$ and $F_{ij}$ ($i$, $j$, $k$=1, 2….6) are strength tensors. The strength coefficients are determined by following conventional strength parameters:

$$F_{11}=\frac{1}{\sigma_{1t}^{*}\sigma_{1c}^{*}},\ F_{22}=\frac{1}{\sigma_{2t}^{*}\sigma_{2c}^{*}},$$
$$F_{1}=\frac{1}{\sigma_{1t}^{*}}-\frac{1}{\sigma_{1c}^{*}},\ F_{2}=\frac{1}{\sigma_{2t}^{*}}-\frac{1}{\sigma_{2c}^{*}},\tag{5}$$
$$F_{44}=\frac{1}{\left(\tau_{23}^{*}\right)^{2}},\ F_{66}=\frac{1}{\left(\tau_{12}^{*}\right)^{2}},\ F_{12}=\frac{1}{2}\sqrt{F_{11}F_{22}}\ .$$

where $\sigma_{1t}^{*}$ and $\sigma_{1c}^{*}$ are the tension and compression along fibre direction; $\sigma_{2t}^{*}$ and $\sigma_{2t}^{*}$ are the tension and compression strengths transverse to fibre direction; and $\tau_{12}^{*}$ and $\tau_{23}^{*}$ are the shear strength parallel and transverse to fibre direction, respectively.

In this section, three stress components, $\sigma_{22}$, $\sigma_{33}$ and $\tau_{12}$, are considered. Therefore, in this stress space, the Tsai-Wu failure criterion Eq. (4) is simplified as

$$F=F_{22}\left(\sigma_{2}^{2}+\sigma_{3}^{2}\right)+\left(2F_{22}-F_{44}\right)\sigma_{2}\sigma_{3}+F_{2}(\sigma_{2}+\sigma_{3})+F_{66}\tau_{12}^{2}\tag{6}$$

The strength parameters of IM7/8552 (lamina) are given in Table 2 [38]. To include the whole failure envelope in the sample space, the range of stress space was defined as

$$\sigma_{2}\in[-600,100],\ \ \sigma_{3}\in[-600,100],\ \ \tau_{12}\in[-300,300].\tag{7}$$

In the work conducted by Yan et al. [28], the sample space covers the entire defined strain space. However, this may bring errors for the ML model. In general, the objective of a ML algorithm is to minimise the loss function [39], and every data point contributes weight for the loss function. Therefore, a large number of data points far away from real decision boundary (RDB) could pull the decision boundary the ML model predicted (PDB) away from the real one, which in return reduces its accuracy( see the 2D case in Fig 4 (a)). For the Tsai-Wu criteria in Eq.(4), the UD composite is safe when $F$<1, which means its decision boundary can be defined as

$$F_{22}\left(\sigma_{22}^{2}+\sigma_{33}^{2}\right)+\left(2F_{22}-F_{44}\right)\sigma_{22}\sigma_{33}+F_{2}(\sigma_{22}+\sigma_{33})+F_{66}\tau_{12}^{2}=1,\tag{8}$$

Table. 2 the strength parameters for IM7/8552 (lamina)

| $\sigma_{2t}^{*}$ (MPa) | $\sigma_{2c}^{*}$ (MPa) | $\tau_{23}^{*}$ (MPa) | $\tau_{12}^{*}$ (MPa) |
|---|---|---|---|
| 62 | 255 | 70 | 100 |

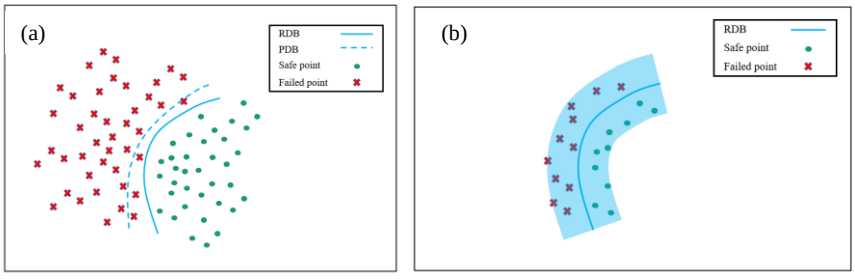


Fig 4. Decision boundary with different types of training data

In order to address this issue, only those data points close to the decision boundary were collected for training in this paper, such that the training set was filtered by

$$1-d<F<1+d\ , \tag{9}$$

The distribution of data points after filtration is illustrated in Fig 4 (b). This can offer a higher accuracy for the ML model, and reduce the volume of training set and the time consumption for training. Furthermore, with this novel data collection strategy, only the data close to critical failure points are needed, therefore significantly reducing the workload for data pre-processing.

In order to verify this strategy, two kinds of training sets（$X^{train}\in R^n, y^{train}$）were generated for comparison. By using Latin hypercube sampling, 10,000 data points were generated in the stress space described by Eq. (7) and were regarded as training set type-I. Similarly, 20,000 data points were generated by using Latin hypercube sampling in the stress space described by Eq. (7) and filtered by Eq. (9) with $d$=0.5. This led to 1282 remaining data points, which were regarded as training set type-II. Another 1000 data points generated by Latin hypercube sampling in the same stress space were used as a testing set（$X^{test}\in R^t, y^{test}$）. Distributions of these data points are shown in Fig 5 and Fig 6.

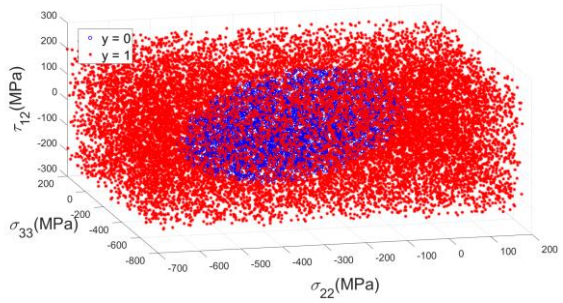


Fig 5. Distribution of data points for training set type-I (y=0 indicates ‘safe’; y=1 indicates ‘failure’).

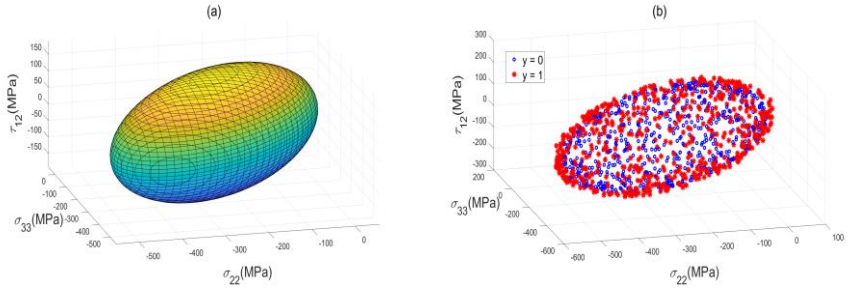


Fig 6. (a) Failure envelop for Tsai-Wu failure criterion in stress space ($\sigma_{22}$, $\sigma_{33}$, $\tau_{12}$); (b) Distribution of data points for training set type-II (y=0 indicates ‘safe’; y=1 indicates ‘failure’).

Both the training and the testing sets were standardised to improve the performance of ML algorithm by

$$\text{Input features}: x=(x_1,x_2,x_3)=\left(\frac{\sigma_{22}-u_2^{train}}{s_2^{train}},\frac{\sigma_{33}-u_3^{train}}{s_3^{train}},\frac{\tau_{12}-u_{12}^{train}}{s_{12}^{train}}\right), \quad (10)$$

$$\text{Output}: y=\{0,1\}$$

where（$u_2^{train}$, $u_2^{train}$, $u_2^{train}$）and（$s_2^{train}$, $s_3^{train}$, $s_{12}^{train}$）are the mean values and standard deviations of the training sets, respectively.

3.2 Verification and comparisons

Three different ML algorithms were selected for evaluation, including Logistic regression, Support vector machine (SVM) and Artificial neural network (ANN). Logistic regression algorithm [40] is one of the most widely used tool for binary classification problems, and has the advantage of simplicity and interpretability. However, it can only work for linearly separable data if the original features are used. Therefore, the original features are normally mapped into new features:

$$\bar{x}=(\bar{x}_1,\bar{x}_2,\bar{x}_3,\bar{x}_4,\bar{x}_5,\bar{x}_6,\bar{x}_7,\bar{x}_8,\bar{x}_9)=(x_1,x_2,x_3,x_1^2,x_2^2,x_3^2,x_1x_2,x_2x_3,x_3x_1), \quad (11)$$

In this paper, the sigmoid function was used as the logistic regression function, and L2 regularisation was adapted for preventing overfitting. The classification rule for prediction rule was defined as:

$$\begin{cases} y_p=0 \quad \text{when} \quad w^T\bar{x}\le 0 \\ y_p=1 \quad \text{when} \quad w^T\bar{x}>0 \end{cases}, \quad (12)$$

where $w$ is the weight vector and $y_p$ is the predicted value.

SVM [41] is another popular algorithm for binary classification problems. It transfers the original features into higher dimension by considering the similarity between different samples, therefore it shows advantage of non-linear classification. The classification rule is defined as:

$$c(x)=\text{sign}(w^T\varnothing(x)+w_0), \quad (13)$$

where $w$ is the weight vector, $w_0$ is the bias term and ø($x$) is the input feature vector transformed from original feature vector by the Gaussian kernel function.

$$k\left(x^{(i)},x^{(j)}\right)=\exp\left(-\frac{\left\|x^{(i)}-x^{(j)}\right\|^2}{2\sigma}\right). \quad (14)$$

ANN [28] is a ML algorithm inspired by brain structure that can deal with non-linear and complex relationships. Besides, it shows good performance on extrapolation and prediction on the relationship among unseen data. In this paper, the ANN model was built on the open-source platform TensorFlow 2.1.0. The ANN model includes an input layer, two hidden layers and an output layer. There are three neurons in the input layer, which are $\sigma_{22}$, $\sigma_{33}$, $\tau_{12}$, and 6 neurons and 12 neurons in first and second hidden layer, respectively.

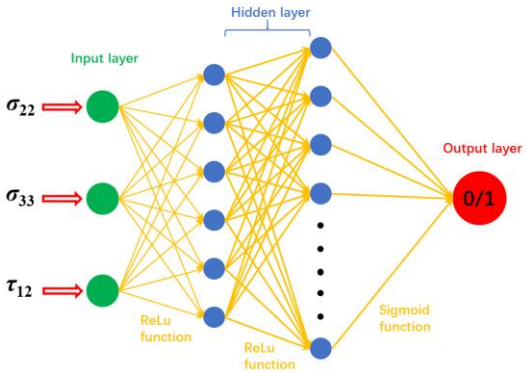


Fig 7. ANN scheme for failure prediction

The Rectified Linear Unit (ReLU) function,

$$R(z) = \max(z, 0) \tag{15}$$

was chosen as activation function in the first layer. The activation function in second hidden layer was the Sigmoid function:

$$S(z) = \frac{1}{1+e^{-z}}. \tag{16}$$

The sigmoid function, as plotted in Fig 8 (a), determines the output in a way such that the output is 1 when sigmoid function exceeds 0.5, otherwise the output is 0. Meanwhile, the confidence of the prediction decreases with the sigmoid function approaching 0.5. In this case, for measuring the confidence of the ANN prediction, a confidence function is introduced:

$$C(z) = \left( \frac{[S(z) - 0.5]}{0.5} \right)^2. \tag{17}$$

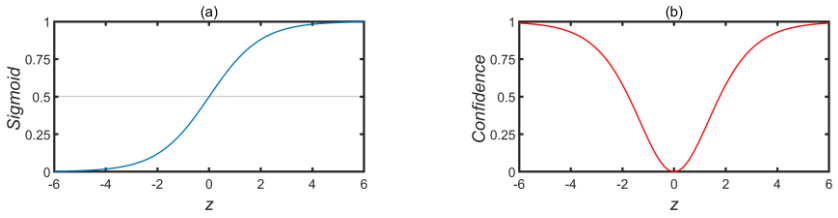


Fig 8. (a) Sigmoid function and (b) Confidence of prediction.

A plot of the confidence function is shown in Fig 8 (b). Furthermore, binary cross entropy loss function,

$$L = -\frac{1}{n}\sum_{i=1}^{n} y_i \log\left(y_p^{(i)}\right) - (1 - y_i)\log\left(1 - y_p^{(i)}\right) \tag{18}$$

combined with Nadam optimisation algorithm [42] was used for training the ANN model, and L2 regularisation was adopted for preventing overfitting. Compared to the logistic regression and SVM algorithm, ANN maps the old features into new features using the activation function in every layer, which offers a highly nonlinear characteristic.

Table. 3. Verification results from different ML algorithms.

| | Training set type-I (10,000 data points) | Training set type-II (1282 data points) |
|---|---|---|
| Logistic regression | 94.0% | 87.0% |
| SVM | 97.5% | 94.9% |
| ANN | 98.3% | 98.1% |

The results in Table. 3~~Table. 3~~ show that ANN offers the highest accuracy in this problem and the accuracy of all three ML algorithms with training set type-II is close to that with training set type-I using much fewer data points. In particular, the ANN maintains a consistent high accuracy when using training set type-II with a smaller training set. As the mechanical response of the RVE under triaxial loads is expected to show high nonlinearity, the ANN with training set type-II were adapted in the following sections for failure prediction.

## 4 Calibration and validation of the RVE-based FE model

In order to obtain the reliable data from the RVE-based FE modelling under triaxial loadings, a parametric study was conducted to identify and calibrate the micro-parameters of the RVE which was further validated by the experimental data from the combined transverse and in-plane biaxial loading states.

### 4.1 Identification of constituent parameters for the RVE model

Due to the absence of some micro-parameters from experiments, a parameter identification plugin tool developed for ABAQUS in our previous work [31] was adopted to identify these parameters. Using the plugin, 1000 samples from Latin hypercube sampling of unit cell RVEs with different micro-parameters were generated and the corresponding macro-parameters were calculated, as illustrated in Fig 9~~Fig 9~~.

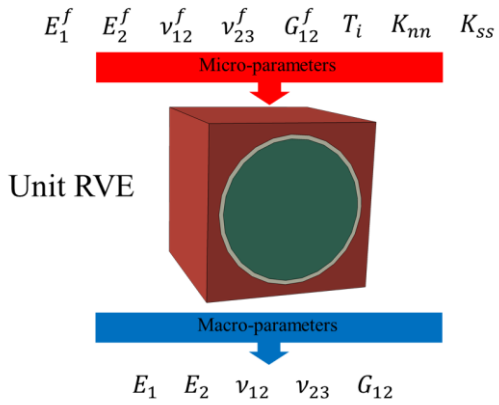


Fig 9. Micro-parameters (Young's modulus $E_1^f$, $E_2^f$, Possion's ratio $\upsilon_{12}^f$, $\upsilon_{23}^f$ shear modulus $G_{12}^f$, of fibre, the thickness $T_i$ and stiffness $K_{nn}$, $K_{ss}$ of interface ) and macro-parameters (Young's modulus $E_1$ , $E_2$ , Poisson's ratio $\upsilon_{12}$, $\upsilon_{23}$ shear modulus $G_{12}$, of UD laminae)

Then, an ANN model is trained with the micro-parameters as the input and macro-parameters as the output. After training, 1,000,000 samples with Latin hypercube sampling was generated by ANN model. The one with the highest similarity of macro-parameters compared to the target material (IM7/8552 UD lamina) was selected, and the similarity was measured using the Euclidean distance function:

$$S=\sqrt{\left(\frac{E_1^s}{E_1}-1\right)^2+\left(\frac{E_2^s}{E_2}-1\right)^2+\left(\frac{\nu_{12}^s}{\nu_{12}}-1\right)^2+\left(\frac{\nu_{23}^s}{\nu_{23}}-1\right)^2+\left(\frac{G_{12}^s}{G_{12}}-1\right)^2}, \tag{19}$$

where $E_1^s$ and $E_2^s$ are the predicted longitudinal and transverse modulus, $\nu_{12}^s$ and $\nu_{23}^s$ are the predicted Poisson's ratio and $G_{12}^s$ is the predicted shear modulus. $E_1$ , $E_2$ , $\nu_{12}$ , $\nu_{23}$ and $G_{12}$ are the material properties of IM7/8552 UD lamina. The identified constituent parameters, together with the experimental ones can be found in Table. 4. As can be seen the macro-parameters of the selected sample agrees with the experimental data extremely well, which means the micro-parameters of the picked sample can be regarded as the identified micro-parameters of the target material.

Commented [YJ4]: Selected?

Table. 4. Elastic parameters of the IM7/8552 UD lamina [38]

| | $E_1$ (GPa) | $E_2=E_3$ (GPa) | $\nu_{12}$ | $\nu_{23}$ | $G_{12}$ (GPa) |
|---|---|---|---|---|---|
| Experiment | 163.0 | 9.0 | 0.32 | 0.5 | 5.17 |
| RVE with identified micro-parameters | 163.2 | 9.0 | 0.32 | 0.5 | 5.0 |

4.2 Calibration of interface strength in the RVE model

Due to the lack of experimental data of the fibre/matrix interface strengths, reverse engineering was adopted based on correlating the RVE predicted ultimate strengths to the experimental data [38] under different uniaxial loadings. As explained in the above section, the interface fracture energies for mode I and mode II were taken as 2 J/m$^2$ [20,34] and 100 J/m$^2$ [20,34,36], respectively. For the parametric study of the interface properties, the stress-strain curves of the RVE model under different loadings can be obtained by varying the interface strengths of mode I from 48 to 58 MPa and of mode II from 82 to 102 MPa, respectively, with a reference to those values used in [36]. It can be found in **Error! Reference source not found.** that when keeping the fracture energy of mode I constant, the interface normal strength shows strong influence on the ultimate strength of the RVE. A value of 58 MPa for the interface strength was observed to give the best match with the experimental tensile strength, compared to the numerical results obtained from the strength values of 48 and 53 MPa. For the sake of simplicity, the in-plane shear strength of the interface was assumed to be equal to its transverse shear strength. After a few trials, it was found that the ultimate in-plane shear strength of the RVE increased with the interface shear strengths. However, the ultimate strength obtained from the interface strength of 102 MPa was only slightly larger than the one from 92 MPa, which is mainly due to the fact that the shear strength is slightly larger than the matrix tensile strength (99 MPa), resulting in the earlier damage in the matrix, instead of the interface failure. Compromising between the compressive and in-plane shear ultimate strengths of the RVE with different interface shear strengths, 92 MPa was adopted in the following numerical simulations of biaxial and triaxial loadings.

**Commented [YJ5]:** Is this strong enough for the assumption?

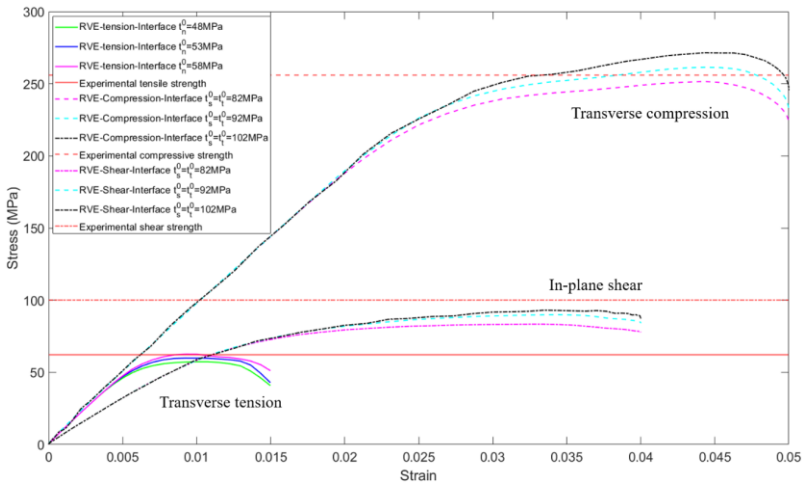


Fig 10. Comparison of failure strengths between experimental data [32] and numerical simulations under tensile, compressive and in-plane shear loadings

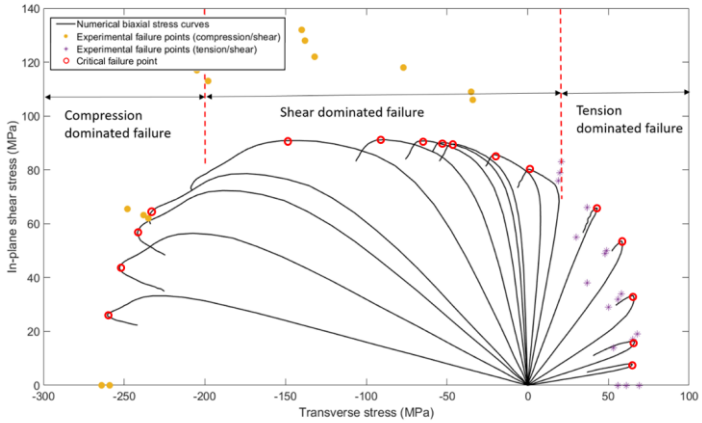


Fig 11. Comparison between the experimental failure points [32] and numerical failure envelope of the RVE model loaded with combined transverse and in-plane shear stress states in $\sigma_{22}$-$\tau_{12}$ stress plane

4.3 Validation of the RVE model under transverse tension/compression and in-plane shear biaxial loads

Once the interface properties had been determined, the RVE model was further validated against experimental findings to assess the calibrated interface properties under biaxial loading conditions. Fig 11 shows the comparison of critical failure points between the experimental data [38] and the predicted failure envelope in the $\sigma_{22}$-$\tau_{12}$ stress plane. Each of the obtained stress curve corresponds to a specific displacement ratio of transverse tension/compression to in-plane shear load. For more details refer to [19]. It should be noted that the critical failure points were collected at the stress reduction points for different dominated failure modes, which means the points of compression stress, shear stress and tension stress were regarded, respectively, as the critical failure points for the compression dominated failure, shear dominated failure and tension dominated failure. Moreover, the region for each failure mode in the $\sigma_{22}$-$\tau_{12}$ stress plane is marked according to the observed dominant failure mode of the RVE when subjected to different biaxial loadings.

**Commented [YJ6]:** Stress ratio?

**Commented [YJ7]:** Points when the respective stresses started declining. Better?

It can be found that the predicted critical failure points agree very well with the experimental data in the compressive and tension dominated failure regions, suggesting that the interface friction has negligible effects in both regions. However, it plays a significant role in the shear dominated region, which causes the shear hardening when the RVE is subjected to a moderate compressive stress. This is believed to result in the big discrepancy between the predicted critical failure points and experiments in the shear dominated region, as shown in Fig 11. Nevertheless, it should also be noted that the aim of this study was to propose a framework for applying the ML techniques to predict the failure of composite materials under multiaxial stress states with the help of RVE modelling. Therefore, with continuing improvement on the RVE model in the future (i.e. consideration of interface friction), more accurate critical failure points would be generated for the training of the ML models.

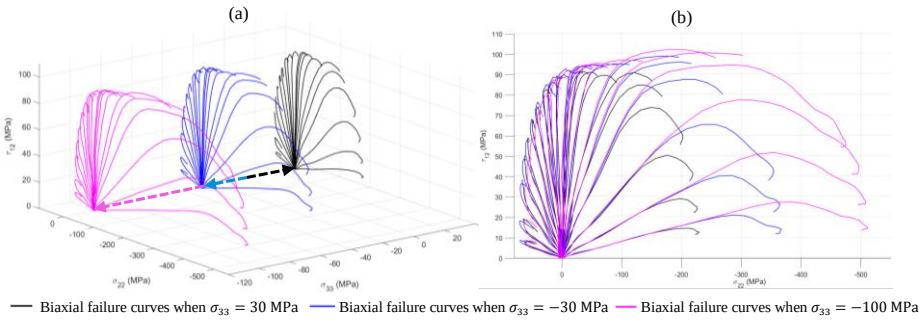


Fig 12. Stress curves from the RVE model under triaxial loads (a) in the ($\sigma_{22}$, $\sigma_{33}$, $\tau_{12}$) stress space and (b) their projections on the $\sigma_{22}$-$\tau_{12}$ stress plane.

4.4 Failure prediction of IM7/8552 UD lamina under triaxial loadings

Failure prediction of the IM7/8552 UD lamina was conducted under $\sigma_{22}$-$\tau_{12}$-$\sigma_{33}$ triaxial loads. Examples of stress curves from the RVE-based FE modelling are presented in Fig 12. A slicing technique was applied in the ($\sigma_{22}$, $\sigma_{33}$, $\tau_{12}$) stress space, with one slice at each $\sigma_{33}$ stress. Due to the symmetry of the failure surfaces in the $\sigma_{22}$-$\sigma_{33}$ stress plane, only the data points on one side were needed from the RVE modelling. In the triaxial loading cases, the loading process was divided into two steps. In the first step, $\sigma_{33}$ was pre-loaded smoothly; in the second step, $\sigma_{22}$ and $\tau_{12}$ were loaded simultaneously, whilst $\sigma_{33}$ was kept constant. Small and moderate stress states of $\sigma_{33}$ in tension and compression were selected to investigate the influences of $\sigma_{33}$ on the failure envelope in the $\sigma_{22}$-$\tau_{12}$ stress plane.

It can be found in Fig 12 (a) that $\sigma_{33}$ has little influence on the combined transverse tension and in-plane shear envelopes, but greater influences on the transverse compression and in-plane shear failure envelopes. To have a better view of this difference, the stress curves were projected to the $\sigma_{22}$-$\tau_{12}$ stress plane, as shown in Fig 12 (b). Specifically speaking, the transverse compressive stresss, $\sigma_{33}$ (blue and pink curves), accelerates the tensile failure in the $x_2$ direction under the biaxial loads, compared to the transverse tensile stress $\sigma_{33}$ (black curves). That is due to the tensile stress in the $x_2$ direction in the matrix, induced by the compressive stress $\sigma_{33}$ through the Poisson's effect, promoting earlier failure when the combined transverse tensile and in-plane shear loads are applied. However, in the ($\sigma_{22}$, $\sigma_{33}$, $\tau_{12}$) stress space, $\sigma_{33}$ shows larger effects on the compressive failure stress than tensile failure stress. The failure stresses obtained in the compressive failure dominated regions on the slice $\sigma_{33}$ =-100 MPa is two times larger than the ones on the slice of $\sigma_{33}$ =30 MPa, but on the contrary it shows negligible change in the tensile failure dominated regions. That is mainly because the biaxial compression may have closed the micro cracks, and thus delaying the compressive failure during the triaxial loadings.

Slices were inserted between $\sigma_{33}$=60 MPa and $\sigma_{33}$=-260 MPa, because the tensile strength and compressive strength are 63MPa and -269 MPa, respectively. The stress states on the slices beyond that range enter the failure region, which are invalid. Due to the cases with a pre-loading $\sigma_{33}$ higher than -220MPa show unstable results, they were not considered in this work, therefore 28 slices in total were taken into account in this study. In every slice, 20 cases with different ratio of $\varepsilon_{22}$ and $\varepsilon_{12}$ were defined, i.e. 560 stress curves were obtained in total.

**Commented [YJ8]:** Is this 270?

**Commented [YJ9]:** Outside?

**Commented [YJ10]:** Not easy to understand. Need to rephrase

**Commented [YJ11]:** Strain?

**5. Data-driven ANN prediction of composites failure**

Before training the ANN model, effective data sets need to be extracted from the stress curves sliced at different $\sigma_{33}$ in the ($\sigma_{22}$, $\sigma_{33}$, $\tau_{12}$) stress space. Firstly, half of critical failure points (560 points) of the stress curves can be identified by checking the stress reduction and the failure modes, and the other half is obtained by mirroring them about the $\sigma_{22}$-$\sigma_{33}$ stress plane, thus 1120 data points in total were collected (see in Fig 13). Because there is a change of failure mode on every slice and the stress curves among slices share identical strain ratios of transverse tension/compression to in-plane shear load, there is a vacant space among the critical failure points in the (-$\sigma_{22}$, -$\sigma_{33}$, $\tau_{12}$) stress space and it becomes enlarged with the increase of the pre-load, $\sigma_{33}$. Another vacant space is in the (-$\sigma_{22}$, -$\sigma_{33}$, $\tau_{12}$) stress space, which is because no more slices are inserted in this direction. These vacancies have limited influence to the training of ANN model, because there will be no significant fluctuation of critical failure points in these vacant spaces.

Commented [YJ12]: Not properly said.

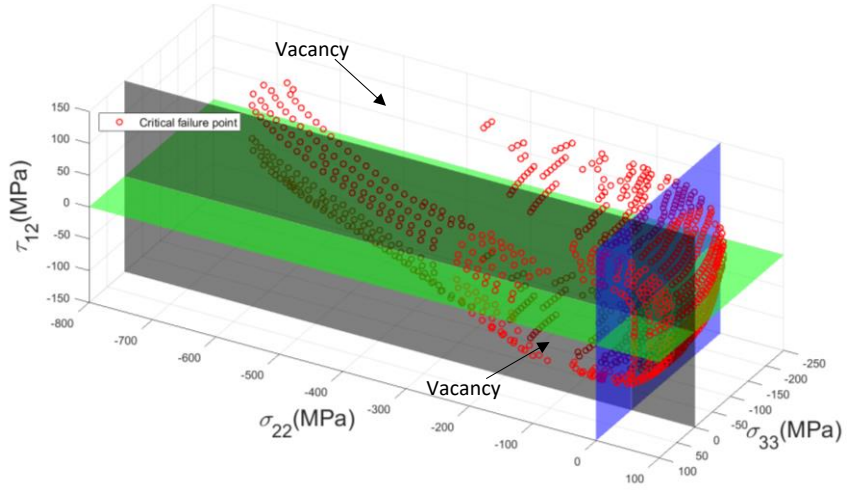


Fig 13. Critical failure points of the RVE in the ($\sigma_{22}$, $\sigma_{33}$, $\tau_{12}$) stress space

Secondly, a radial loading path was drawn, starting from the original point and passing through every critical failure point in each slice. In our previous work and other reported studies in literature [14,43–46], the failure patterns were found to be independent from the loading paths. Therefore, the points before the critical failure point on the radial loading path can be regarded as safe points, and those after the critical failure point are regarded as failure points. As such, two failure points and two safe points close to the critical failure point were generated and collected for later training of the ANN, resulting in 2240 safe points and 2240 failure points in total as illustrated in Fig 14.

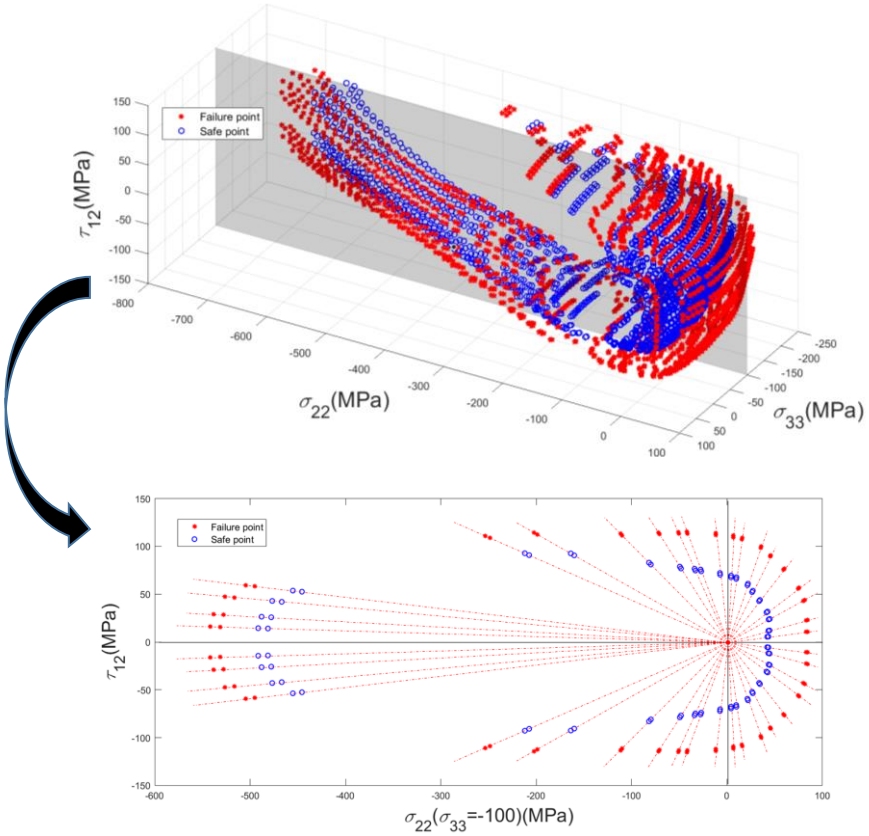


Fig 14. Training sets extracted from RVE modelling for the ANN training

Twelve points, including those two points from the training set, on every radial path beyond the critical failure point were collected as failure points (i.e.13440 points) and for the balance of the weight between the safe points and the failure points, 13440 points on the failure curves before the critical points were randomly collected as safe points as illustrated in Fig 15. Of these safe points and failure points, 20 % were used as the validation set while 80 % were used as validation set.

**Commented [YJ13]:** Both are validation sets?

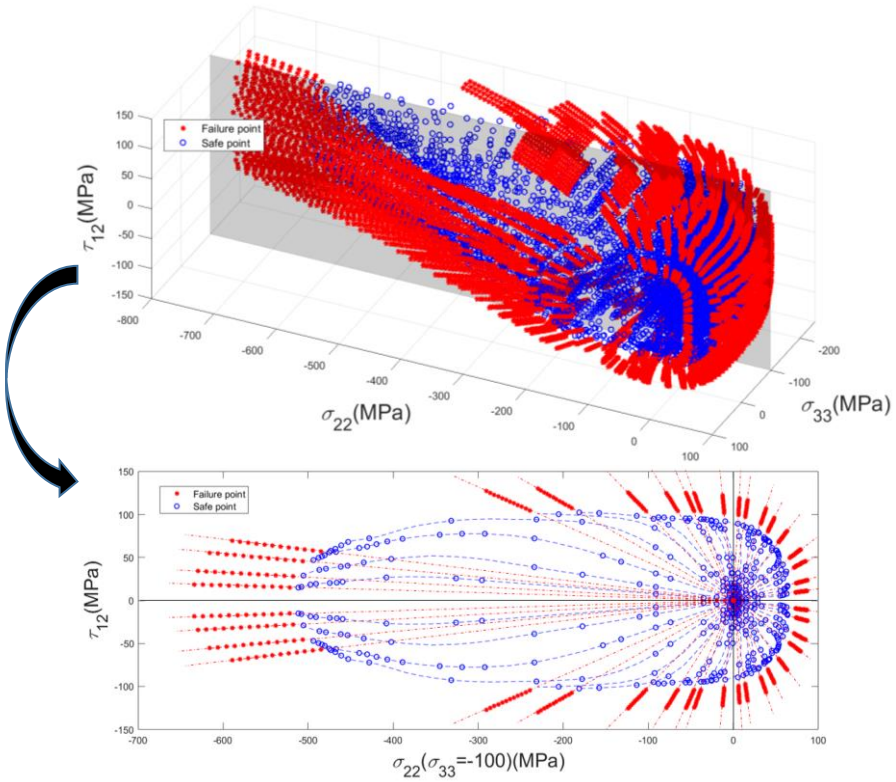


Fig 15. Data sets extracted from the RVE modelling for test and validation of the ANN model

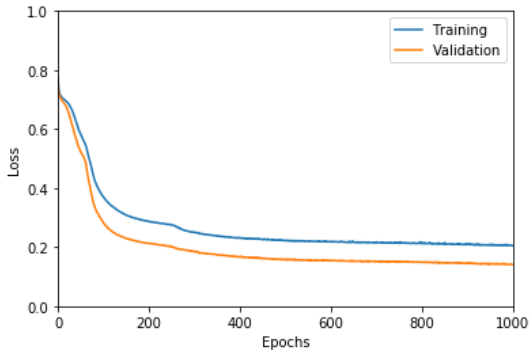


Fig 16. Training loss and validation loss across epochs.

Once the data sets were selected, the ANN model described in Section 3.1 was trained, validated and tested. It can be found in Fig 16 that the training and validation loss decreased with epochs and converged after 600 epochs with no overfitting issue. Finally, the accuracy of ANN model on the testing set reached 97.5%.

In order to visualise the decision boundary of the ANN model, around 630,000 data points were sprinkled evenly in the stress space $\sigma_{22} \in$ (-800Mpa, 100Mpa), $\sigma_{33} \in$ (-300Mpa, 100Mpa), $\tau_{12} \in$ (-150Mpa, 150Mpa), and then the sigmoid function Eq. (16) in the output layer of ANN model was calculated using the trained ANN model for every data point. After that, an iso-surface for $S(z)$=0.5 can be constructed, which is the predicted failure surface for the IM7/8552 UD laminae, as shown in

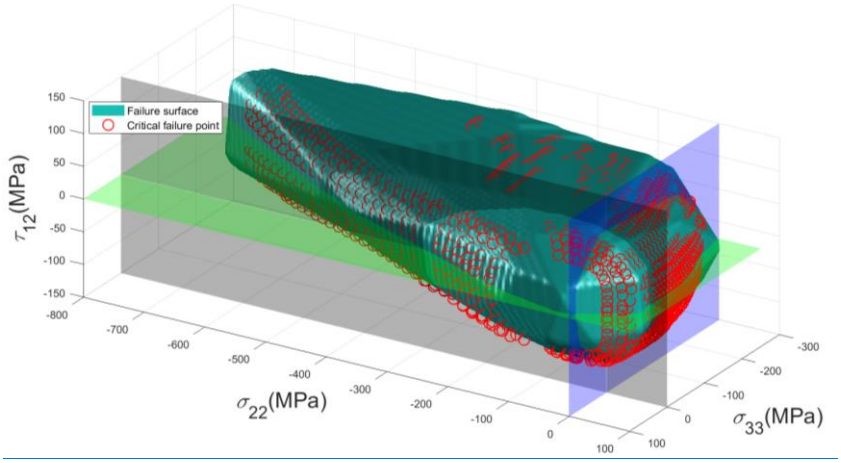


Fig 17. The predicted failure surface turned out to be an elliptical paraboloid, where the failure strength in the ($-\sigma_{22}$, $-\sigma_{33}$, $\tau_{12}$) stress space is much larger than that in the ($+\sigma_{22}$, $+\sigma_{33}$, $\tau_{12}$) stress space. As can be seen the failure surface in the ($\sigma_{22}$, $-\sigma_{33}$, $\tau_{12}$) stress space is open, and there is a growing tendency for failure strength with the increase of biaxial compression stresses, which agrees with the infinite strength assumption for equal biaxial transverse compression proposed by Hashin [3]. Besides, the predicted failure surface is in good agreement with the critical failure points, demonstrating the trained ANN model offers a high accuracy for predicting the failure strength in the ($\sigma_{22}$, $\sigma_{33}$, $\tau_{12}$) stress space concerned in this study.

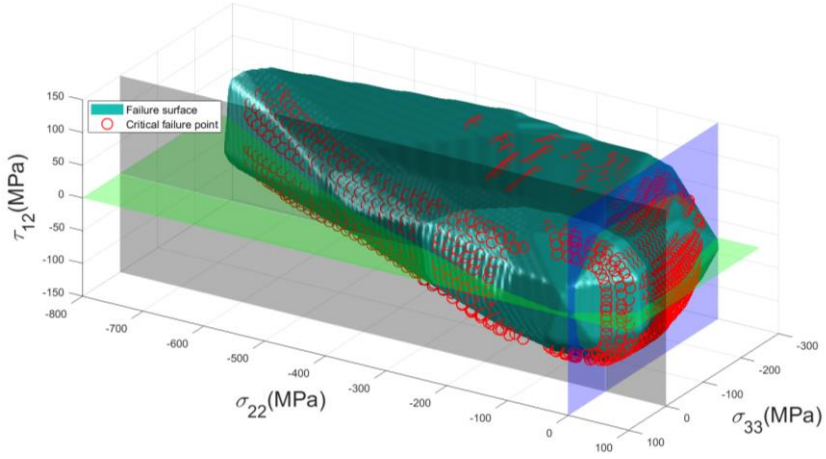

Fig 17. ANN predicted failure surface in the ($\sigma_{22}$, $\sigma_{33}$, $\tau_{12}$) stress space

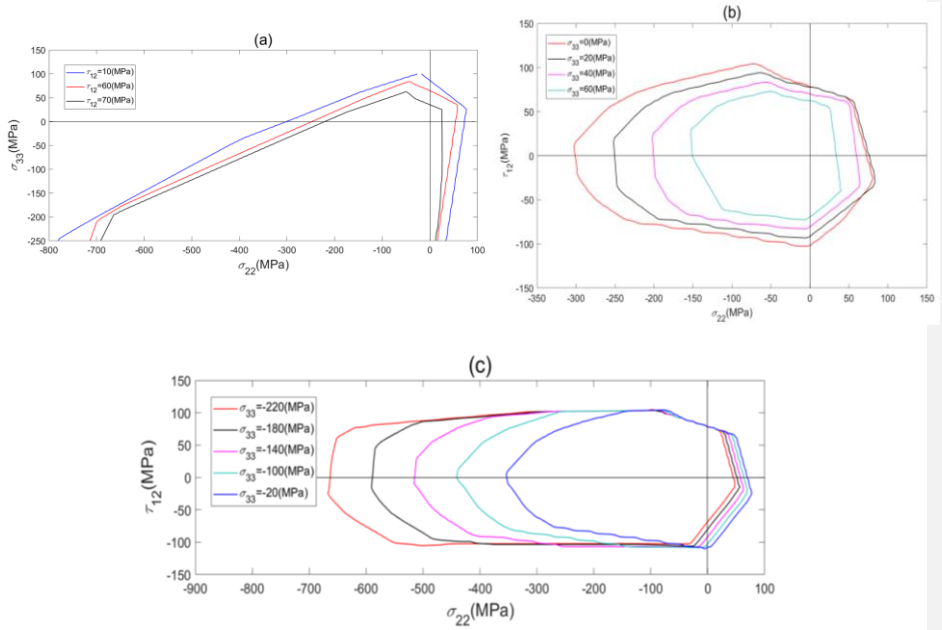


Fig 18. 2D cross-planes from the predicted 3D failure surface

Based on the predicted failure surface, slices perpendicular to the $\sigma_{33}$ and $\tau_{12}$ directions are plotted in Fig 18 to show the evolution of the 2D failure envelopes. Due to that the failure surface is symmetric about the $\sigma_{22}$-$\sigma_{33}$ plane, only the slices in $\tau_{12} \in$ (0Mpa, 120Mpa) are plotted. It has been seen in Fig 18 (a) that the failure envelopes in the ($\sigma_{22}$, $\sigma_{33}$) stress region shrink with the increase of $\tau_{12}$, which is mainly because $\tau_{12}$ could introduce micro-damage to the composite and reduce the final compression strength. Similar phenomenon also occur in the failure envelopes in the ($\sigma_{22}$, $\tau_{12}$) stress region in Fig 18 (b), where the increase of $+\sigma_{33}$ results in lower compression or shear strength. Another interesting observation from Fig 18 (a) is that with the increase of $\tau_{12}$, the failure envelops shifts to the ($-\sigma_{22}$, $-\sigma_{33}$) stress region, suggesting that the shear strength increase with the increase of $-\sigma_{22}$ and $-\sigma_{33}$. This is because the biaxial compression supressed the matrix and interface, resulting in a higher fracture energy for shear failure. In Fig 18 (c), with the increase of $-\sigma_{33}$, the tensile strength decreases, while the compressive strength increases dramatically. This is mainly because $-\sigma_{33}$ induces tensile deformation in the $+\sigma_{22}$ direction as the result of the Poisson's effect, which leads to a lower needed $+\sigma_{22}$ for the interface failure. However, for the compressive strength $-\sigma_{22}$, biaxial compression can compact the composite and improve the compressive strength. Due to the symmetry of $\tau_{12}$, the failure surface should be symmetrical about the $\sigma_{22}$-$\sigma_{33}$ stress plane, but the cross-planes for the predicted failure surface Fig 18 (b) and (c) are not perfectly symmetrical because of the errors from ANN model training and iso-surface calculation.

## 6. Conclusions

A general framework of applying ML techniques associated with micromechanics based FE analysis was proposed to predict the failure of the IM7/8552 UD lamina subjected to $\sigma_{22}$-$\tau_{12}$-$\sigma_{33}$ triaxial loads. An RVE-based FE model was established using three phases (fibre, matrix and interface) and loaded by means of periodic boundary conditions following a hybrid loading strategy. The microscale parameters used in the RVE model, such as the fibre elastic parameters and interface thickness and stiffnesses were identified using a plugin developed in the ABAQUS$^{TM}$ together with ML techniques. A coupled numerical-experimental methodology was employed to calibrate the interface properties and validate the RVE model. Failure prediction of the UD lamina subjected to triaxial loadings was conducted by employing the RVE model. Triaxial critical failure points were collected to reconstruct the failure surface of UD lamina under triaxial loadings with a shallow ANN model. The main conclusions of the study are summarized as follows:

- A three-phase RVE model was established with identified constituent parameters. The uniaxial strength and the biaxial strength for tension dominated compression dominated failure show good agreement with experiment data. However, the lack of friction between fractured fibre/matrix interfaces may lead to reduced accuracy of the RVE model for capturing the shear strength hardening under moderate compressive stresses.
- Transverse stress ($\sigma_{33}$) in one direction has little influences on the ($+\sigma_{22}$, $\tau_{12}$) stress region, while has great influences on the ($-\sigma_{22}$, $\tau_{12}$) stress region.
- Using limited data close to the failure surface can provide high enough accuracy for failure prediction with shallow ANN model compared to using the large number of data with random distribution.
- The ANN model appeared to be reasonably robust for the failure prediction of composite laminae. Based on the critical failure points extracted from the RVE-based FE modelling in the ($\sigma_{22}$, $\sigma_{33}$, $\tau_{12}$) stress space, a high-accuracy ANN model is trained with only 560 samples and can offer 97.5% accuracy.
- The failure surface constructed based on the trained ANN model turned out to be elliptical paraboloid, in which the failure strength in ($-\sigma_{22}$, $-\sigma_{33}$, $\tau_{12}$) stress space was much higher than that in ($+\sigma_{22}$, $+\sigma_{33}$, $\tau_{12}$) stress space. It is noticed that the triaxial strength reduce with the increase of $\tau_{12}$ or $+\sigma_{33}$, the shear strength increases with $-\sigma_{22}$ and $-\sigma_{33}$ involved, furthermore, the tensile strength decreased and the compressive strength increased with the increase of $-\sigma_{33}$.

A more high-fidelity FE model, particularly considering the friction between fibres and matrix should be developed in the future work to capture the shear hardening under moderate compressive stresses. A more reliable matrix constitutive model should be adopted since it would have large effects on the determining the ultimate strength of the RVE model. In the future, this work will be extended to the failure prediction with more than three stress components, e.g. ambitiously all six stress components, such that a failure criterion can be integrated in an ANN model. Eventually, the failure criterion can be implemented into a FEM software for composites failure analysis and design.

**Acknowledgement**

The first two authors (JC and LW) would like to thank China Scholarship Council (CSC) for sponsoring their studies.

**References**

[1] Hart-Smith LJ. Predictions of the original and truncated maximum-strain failure models for certain fibrous composite laminates. Compos Sci Technol 1998;58:1151–78.

[2] Christensen RM. Tensor Transformations and Failure Criteria for the Analysis of Fiber Composite Materials. J Compos Mater 1988;22:874–97.

[3] Hashin Z. Failure Criteria for Unidirectional Fiber Composites. J Appl Mech 1980;47:329–34.

[4] Christensen RM. Stress based yield/failure criteria for fiber composites. Int J Solids Struct 1997;34:529–43.

[5] Sun C, Tao J, Kaddour AS. The prediction of failure envelopes and stress/strain behavior of composite laminates: Comparison with experimental results. Compos Sci Technol - Compos SCI TECHNOL 2002;62:1673–82.

[6] Puck A, Schürmann H. Failure Analysis of Frp Laminates by Means of Physically Based Phenomenological Models. Compos Sci Technol 2002;58:1633–62.

[7] Davila CG, Camanho PP, Rose CA. Failure Criteria for FRP Laminates. J Compos Mater 2005;39:323–45.

[8] Pinho S, Iannucci L, Robinson P. Physically-based failure models and criteria for laminated fibre-reinforced composites with emphasis on fibre kinking: Part I: Development. Compos Part A Appl Sci Manuf 2006;37:63–73.

[9] Hinton MJ, Soden PD. Predicting failure in composite laminates: the background to the exercise. Compos Sci Technol 1998;58:1001–10.

[10] Kaddour AS, Hinton MJ. Maturity of 3D failure criteria for fibre-reinforced composites: Comparison between theories and experiments: Part B of WWFE-II. J Compos Mater 2013;47:925–66.

[11] Kaddour AS, Hinton MJ, Smith PA, Li S. Mechanical properties and details of composite laminates for the test cases used in the third world-wide failure exercise. J Compos Mater 2013;47:2427–42.

[12] Kaddour AS, Hinton MJ, Smith PA, Li S. A comparison between the predictive capability of matrix cracking, damage and failure criteria for fibre reinforced composite laminates: Part A of the third world-wide failure exercise. J Compos Mater 2013;47:2749–79.

[13] Daniel IM. Yield and failure criteria for composite materials under static and dynamic loading. Prog Aerosp Sci 2016;81:18–25.

[14] Sun Q, Zhou G, Meng Z, Guo H, Chen Z, Liu H, et al. Failure criteria of unidirectional carbon fiber reinforced polymer composites informed by a computational micromechanics model. Compos Sci Technol 2019;172:81–95.

[15] Varga C, Miskolczi N, Bartha L, Lipóczi G. Improving the mechanical properties of glass-fibre-reinforced polyester composites by modification of fibre surface. Mater Des 2010;31:185–93.

[16] González C, LLorca J. Mechanical behavior of unidirectional fiber-reinforced polymers under transverse compression: Microscopic mechanisms and modeling. Compos Sci Technol 2007;67:2795–806.

[17] Totry E, González C, LLorca J. Failure locus of fiber-reinforced composites under transverse compression and out-of-plane shear. Compos Sci Technol 2008;68:829–39.

[18] Canal LP, Segurado J, LLorca J. Failure surface of epoxy-modified fiber-reinforced composites under transverse tension and out-of-plane shear. Int J Solids Struct 2009;46:2265–74.

[19] Wan L, Ismail Y, Zhu C, Zhu P, Sheng Y, Liu J, et al. Computational micromechanics-based prediction of the failure of unidirectional composite lamina subjected to transverse and in-plane shear stress states. J Compos Mater 2020;54:3637–54.

[20] Naya F, González C, Lopes CS, Van der Veen S, Pons F. Computational micromechanics of the transverse and shear behavior of unidirectional fiber reinforced polymers including environmental effects. Compos Part A Appl Sci Manuf 2017;92:146–57.

[21] Totry E, González C, LLorca J. Prediction of the failure locus of C/PEEK composites under transverse compression and longitudinal shear through computational micromechanics. Compos Sci Technol 2008;68:3128–36.

[22] Romanowicz M. A numerical approach for predicting the failure locus of fiber reinforced composites under combined transverse compression and axial tension. Comput Mater Sci 2012;51:7–12.

[23] Lu J, Zhu P, Ji Q, Feng Q, He J. Identification of the mechanical properties of the carbon fiber and the interphase region based on computational micromechanics and Kriging metamodel. Comput Mater Sci 2014;95:172–80.

[24] Mangalathu S, Jeon JS. Classification of failure mode and prediction of shear strength for reinforced concrete beam-column joints using machine learning techniques. Eng Struct 2018;160:85–94.

[25] Huang H, Burton H V. Classification of in-plane failure modes for reinforced concrete frames with infills using machine learning. J Build Eng 2019;25:100767.

[26] Liu X, Gasco F, Goodsell J, Yu W. Initial failure strength prediction of woven composites using a new yarn failure criterion constructed by deep learning. Compos Struct 2019;230:111505.

[27] Liu X, Athanasiou CE, Padture NP, Sheldon BW, Gao H. A machine learning approach to fracture mechanics problems. Acta Mater 2020;190:105–12.

[28] Yan S, Zou X, Ilkhani M, Jones A. An efficient multiscale surrogate modelling framework for composite materials considering progressive damage based on artificial neural networks. Compos Part B Eng 2020;194:108014.

[29] Soden PD, Hinton MJ, Kaddour AS. Lamina properties, lay-up configurations and loading conditions for a range of fibre-reinforced composite laminates. Compos Sci Technol 1998;58:1011–22.

[30] Ismail Y, Yang D, Ye J. Discrete element method for generating random fibre distributions in micromechanical models of fibre reinforced composite laminates. Compos Part B Eng 2016;90:485–92.

[31] Ismail Y, Wan L, Chen J, Ye J, Yang D. An ABAQUS® plug-in for generating virtual data required for inverse analysis of unidirectional composites using artificial neural networks. Compos Struct. (submitted)

[32] Ward IM. Review: The yield behaviour of polymers. J Mater Sci 1971;6:1397–417.

[33] Fiedler B, Hojo M, Ochiai S, Schulte K, Ando M. Failure behavior of an epoxy matrix under different kinds of static loading. Compos Sci Technol 2001;61:1615–24.

[34] Melro AR, Camanho PP, Andrade Pires FM, Pinho ST. Micromechanical analysis of polymer composites reinforced by unidirectional fibres: Part II – Micromechanical analyses. Int J Solids Struct 2013;50:1906–15.

[35] Lubliner J, Oliver J, Oller S, Oñate E. A plastic-damage model for concrete. Int J Solids Struct 1989;25:299–326.

[36] Jeeho L, L. FG. Plastic-Damage Model for Cyclic Loading of Concrete Structures. J Eng Mech 1998;124:892–900.

[37] Tsai SW, Wu EM. A General Theory of Strength for Anisotropic Materials. J Compos Mater 1971;5:58–80.

[38] Koerber H. Mechanical Response of Advanced Composites under High Strain Rates 2010:262.

[39] Wang Q, Ma Y, Zhao K, Tian Y. A Comprehensive Survey of Loss Functions in Machine Learning. Ann Data Sci 2020.

[40] Ezukwoke K, Zareian S. LOGISTIC REGRESSION AND KERNEL LOGISTIC REGRESSION A comparative study of logistic regression and kernel logistic regression for binary classification. 2019.

[41] Huang H, Burton H V. Classification of in-plane failure modes for reinforced concrete frames with infills using machine learning. J Build Eng 2019;25:100767.

[42] Dozat T. Incorporating Nesterov momentum into Adam, in: Proceedings of the International Conference on Learning Representation, 2018.

[43] Chen J, Wan L, Ismail Y, Hou P, Ye J, Yang D. Numerical analysis of loading path effects on the failure strength of unidirectional carbon fibre reinforced polymer composite laminae under multiaxial loading. Compos Struct. (submitted)

[44] Choo VKS. Effect of Loading Path on the Failure of Fibre Reinforced Composite Tubes. J Compos Mater 1985;19:525–32.

[45] Totry E, González C, Llorca J. Influence of the Loading Path on the Strength of Fiber-Reinforced Composites Subjected to Transverse Compression and Shear. Int J Solids Struct 2008;45.

[46] Vogler TJ, Kyriakides S. Inelastic behavior of an AS4/PEEK composite under combined transverse compression and shear. Part I: experiments. Int J Plast 1999;15:783–806.